Chemical Engineering Journal 442 (2022) 136207

Contents lists available at ScienceDirect

Chemical Engineering Journal

journal homepage: www.elsevier.com/locate/cej

Versatile CMPs as platforms to support Ag nanocatalysts for nitrophenol hydrogenation in continuous flow-through process

Songhao Luo [a,b,c,d,1], Zhifeng Liu [a,b,c,d,1], Yang Liu [a,b,c,d,1], Eydhah Almatrafi [d,1], Binbin Shao [b,c], Biao Song [a,b,c,d], Chengyun Zhou [a,b,c,d], Yukui Fu [b,c], Miao He [b,c], Zhuotong Zeng [a,b,c,d,*], Guangming Zeng [a,b,c,d,*]

[a] Department of Dermatology, Second Xiangya Hospital, Central South University, Changsha 410011, PR China
[b] College of Environmental Science and Engineering, Hunan University, Changsha 410082, PR China
[c] Key Laboratory of Environmental Biology and Pollution Control, Hunan University, Ministry of Education, Changsha 410082, PR China
[d] Center of Research Excellence in Renewable Energy and Power Systems, Center of Excellence in Desalination Technology, Department of Mechanical Engineering, Faculty of Engineering-Rabigh, King Abdulaziz University, Jeddah 21589, Saudi Arabia

ARTICLE INFO

Keywords:
Conjugated microporous polymers
Catalytic hydrogenation
Water treatment
Flow-through
Silver nanocatalysts

ABSTRACT

4-nitrophenol (4-NP) in industrial wastewater is harmful to both ecological environment and human health even in the very low concentration in the environment. Catalytic hydrogenation, which converts toxic pollutants from wastewater into high-value industrial feedstocks, is a coveted treatment option, but the design of suitable catalysts has been a challenge in the field. In this work, the functionalized conjugated microporous polymers (CMPs) anchored Ag nanocatalysts could effectively catalyze the hydrogenation of 4-NP in wastewater to 4-aminophenol (4-AP) with the rate constant k of 0.01544 s^{-1}. We further optimized the morphology of the CMP substrate to stabilize Ag nanocatalysts and integrated the composite into a modular unit for continuous flow wastewater treatment with an outstanding permeation flux of 1603 L $m^{-2}h^{-1}$ (LMH). These findings provide an effective strategy to design noble metal catalysts for catalytic hydrogenation and could potentially be modularized for use in mountainous and isolated communities.

1. Introduction

4-nitrophenol (4-NP) in industrial wastewater is considered to cause serious damage to the water environment, and its concentration is usually much higher than 500 mg/L [1–3], so the treatment of 4-NP in water is a theme of widespread concern [4–6]. This provides an exciting opportunity to explore effective methods for the reduction of 4-NP in water. Among them, hydrogenation reduction reaction has strong operability and high efficiency [7–9], and is considered as the most effective reduction technology of 4-NP. Meanwhile, the product of hydrogenation reduction of 4-NP is 4-aminophenol (4-AP), which is a beneficial precursor for the synthesis of drugs, desiccants, and corrosion inhibitors, and provides higher economic benefit [10–12]. Currently, the main obstacle in the removal of 4-NP from water by hydrogenation is how to obtain a suitable catalyst.

Fine noble metal catalysts proved to be highly efficient atomic materials with high density of catalytic active sites [13–17]. The catalytic activity of noble metal catalysts strongly depends on the catalytic active atoms on the catalyst surface, how to maximize the efficiency of metal atoms, which is particularly important to improve the catalytic activity of noble metal catalysts. Therefore, researchers tend to synthesize noble metal catalysts with finer structures [18–20]. However, as the size of the noble metal catalyst decreases, its surface energy increases [21], and then noble metal catalysts tend to aggregate during the catalytic process [22,23], thus reducing the catalytic activity and efficiency. Despite extensive research work [24–26], highly efficient synthetic methods to achieve ultrafine metal nanocatalysts or single-atom catalysts are rare and highly desirable.

With the development of polymer science, the emergence of porous organic polymers (POPs) provides a platform for fine noble metal catalysts anchoring [27–31]. The porous substrate has a high surface area, which can increase the reachable catalytic active site and the chance of

* Corresponding authors at: Department of Dermatology, Second Xiangya Hospital, Central South University, Changsha 410011, PR China.
E-mail addresses: zengzhuotong@csu.edu.cn (Z. Zeng), zgming@hnu.edu.cn (G. Zeng).
[1] These authors contribute equally to this article.

https://doi.org/10.1016/j.cej.2022.136207
Received 5 January 2022; Received in revised form 20 March 2022; Accepted 2 April 2022
Available online 5 April 2022

contact between the catalytic active site and the reactants. As well, the porous substrate can subtly control the nucleation and growth of noble metal nanocatalyst, keep the fine size of a noble metal catalyst, and synthesize nanocatalyst with consistent size and stability. Furthermore, in specific and confined spaces, catalytic reactions may exhibit better catalytic performance due to the confinement effects [32–35]. Among them, conjugated microporous polymers (CMPs) [36–40] can be flexibly adjusted and modified to change their morphology and chemical properties to meet special application requirements, and have inherent microporous properties and coherent pores provided by gelation to provide transport channels and accessible catalytic active sites for reactants [41–43]. In consequence, CMPs may be a reasonable candidate for the fine synthesis of metal nanocatalysts.

Herein, the most classical bipyridine-based CMP was redesigned with a robust 3D network and bipyridine coordination groups, which were viable coordination groups for trapping Ag ions [44–46]. In the subsequent reduction process, the CMPs played the role of confinement and immobilization, promoting the fine synthesis of noble metal nanocatalyst. Through the analysis of the synthesis results, we found that compared with the $NaBH_4$ reduction method, the photoreduction method could obtain finer nanostructures. Subsequently, the Ag@CMP composites were further developed for the treatment of 4-NP in water, showing outstanding catalytic activity and stability. Furthermore, to verify the effect of monomer type and proportion on CMP morphology, we synthesized processable CMP aerogels loaded with Ag nanocatalysts by adjusting the reaction solvent, monomer type and ratio, which is crucial for practical water treatment applications.

2. Experiments

2.1. Chemicals

1,3,5-Triethynylbenzene was obtained from TCI. 5,5′-Dibromo-2,2′-bipyridyl (synthetic process [47]) was purchased from Aladdin, 1H NMR ($CDCl_3$) δ (ppm): 7.94 (dd, 2H), 8.27 (d, 2H), 8.70 (d, 2H); 13C NMR ($CDCl_3$) δ (ppm): 121.46, 122.23, 139.61, 150.29, 153.68. Elemental combustion analysis (%) Calcd for $C_{10}H_6N_2Br_2$: C, 38.25; H, 1.93; N, 8.92; Br, 50.90; Found: C, 38.01; H,1.99; N, 8.73. 4,4′-Dibromobiphenyl was purchased from Alfa Aesar. Tetrakis(triphenylphosphine)palladium (0) was obtained from Aldrich. Copper(I) iodide, ammonium persulfate, silver nitrate ($AgNO_3$), concentrated sulfuric acid, and all organic solvent (AR) such as dimethyl formamide (DMF), triethylamine (Et_3N), toluene, trichloromethane, acetone, methanol, and ethanol, etc. were all purchased from Aladdin and without further purification.

2.2. Synthesis of functionalized CMP substance

1,3,5-Triethynylbenzene (300.36 mg, 2 mmol), 5,5′-Dibromo-2,2′-bipyridyl (2 mmol, 627.96 mg), 4,4′-Dibromobiphenyl (4 mmol, 1248 mg), tetrakis-(triphenylphosphine)palladium(0) (45 mg), and copper(I) iodide (20 mg) were dissolved in a mixture of Dimethyl Formamide (DMF, 25 mL) and Et_3N (25 mL). N_2 is continuously pumped through the reactor to rigorously exclude oxygen, preventing any homocoupling of the alkyne monomers. In the atmosphere of nitrogen, the mixture was stirred by magnetic force, and the temperature was slowly raised to 90℃. After continuous heating at 90℃ for a period, agitation was stopped when polymerized solids were observed in the reaction system, and the stirrer was sucked out with a strong magnet. After that, the reaction continued at 90℃ for 72 h. At the end of the reaction, the sample is carefully removed and the precipitated reticular polymer is filtered and washed repeatedly with chloroform, water, methanol, and acetone to remove unreacted monomer or catalyst residue. The obtained sample was then extracted by methanol Soxhlet extraction for 48 h to further purification of the polymer. Finally, the yellow product was dried in vacuum for 24 h at 70 °C to obtained CMP-bpybph.

The CMP-bpy network was synthesized by the same method as CMP-bpybph. 1,3,5-Triethynylbenzene (300.36 mg, 2 mmol), 5,5′-Dibromo-2,2′-bipyridyl (470.97 mg, 1.5 mmol), tetrakis-(triphenylphosphine) palladium(0) (30 mg), copper(I) iodide (15 mg), DMF (10 mL) and Et_3N (10 mL) were used in this polymerization. The ratio of alkyne to bromine in CMP-bpy network was subsequently adjusted to 3:1. 1,3,5-Triethynylbenzene (300.36 mg, 2 mmol), 5,5′-Dibromo-2,2′-bipyridyl (313.98 mg, 1 mmol), tetrakis-(triphenylphosphine)palladium(0) (30 mg), copper(I) iodide (15 mg), DMF (10 mL) and Et_3N (10 mL) were used in this polymerization.

100 mg of CMP-bpybph was soaked with ethanol and filtered to remove the ethanol to make CMP-bpybph in a semi-dry state. The soaked CMP-bpybph was then immersed in 100 mL $(NH_4)_2S_2O_8$ saturated 1 mol/L sulfuric acid solution and stirred for 24 h. After the reaction, wash CMP-bpybph with a large amount of distilled water until the washing solution is neutral. Finally, hydrophilic CMP-bpybph (HCMP-bpybph) was obtained by drying at 70℃ all night.

2.3. Preparation of Ag@CMP composite materials

50 mg HCMP-bpybph was added to 50 mL of 10 mmol/L $AgNO_3$ solution, and stirred overnight in the dark. Gray-yellow samples were filtered and collected, cleaned with deionized water for several times, then added to 50 mL of deionized water, and reacted under visible light irradiation for 4 h. In the photoinduced reaction, Ag ions were reduced to Ag NPs in situ to form HCMP-bpybph supported ultrafine Ag NPs (Ag@HCMP-bpybph) composite. 50 mg CMP-bpy was added to 50 mL of 1 mmol/L $AgNO_3$ solution, 100 mg $NaBH_4$ was added and stirred for another 8 h to obtain bipyridine CMP supported Ag nanocatalyst (Ag@CMP-bpy) after stirring in the dark for 4 h. Filtrate and recycle the product, wash it with distilled water three times, and dry them overnight at 60℃ in vacuum to get dry Ag@HCMP-bpybph and Ag@CMP-bpy composite material.

2.4. Preparation of processable Ag@CMP aerogel material

For increase the processibility of the CMP materials, the synthesis process in the previous literature [45,48] was improved, and the ratio of acetylene group and bromine group was adjusted to 2:1 in the synthesis process [49,50]. 1,3,5-Triethynylbenzene (300.36 mg, 2 mmol), 4,4′-Dibromobiphenyl (1.5 mmol, 468.03 mg), tetrakis-(triphenylphosphine) palladium(0) (50 mg), and copper(I) iodide (50 mg) were dissolved in a mixture of toluene (8 mL) and Et_3N (8 mL). N_2 is continuously pumped through the reactor to rigorously exclude oxygen. In the atmosphere of nitrogen, the mixture was stirred by magnetic force, and the temperature was slowly raised to 80℃. After continuous heating at 80℃ for a period, agitation was stopped when polymerized solids were observed in the reaction system, and the stirrer was sucked out with a strong magnet. After that, the reaction continued at 80℃ for 72 h. At the end of the reaction, the sample is carefully removed and the precipitated reticular polymer is filtered and washed repeatedly with chloroform, water, methanol, and acetone to remove unreacted monomer or catalyst residue.

The obtained sample was then extracted by methanol Soxhlet extraction for 48 h to further purification of the polymer. Finally, the yellow product was dried in vacuum for 24 h at 70 °C to obtained CMPA-bph. 100 mg the obtained CMP aerogel (CMPA-bph) was added to 100 mL of 1 mmol/L $AgNO_3$ solution, 200 mg $NaBH_4$ was added and stirred for another 8 h to obtain processable CMP supported Ag nanocatalyst (Ag@CMPA-bph) after stirring in the dark for 4 h. Filtrate and recycle the product, wash it with distilled water three times, and dry them overnight at 60℃ in vacuum to get dry Ag@CMPA-bph material.

2.5. General methods for characterization

Fourier transform infrared spectroscopy (FT-IR) were recorded on KBr disks in transmission mode in the wave number range of 400 ~

4000 cm^{-1} using a ThermoFisher IS5 infrared spectrometer. Solid-state ^{13}C cross polarization magic angle spinning nuclear magnetic resonance (^{13}C CP/MAS NMR) spectra operating at 100.62 MHz for ^{13}C. Powder X-ray diffraction (PXRD) measurement of samples were carried out over the 2θ range of 5°-80° on a Bruke D8 Advance diffraction. Raman spectra were collected on a laser micro-Raman spectrometer (Thermo Fisher DXR) with a laser source of 532 nm. Scanning electron microscopy (SEM) was conducted with Zeiss Sigma 300 microscope. Elemental analyses (C, N, and Ag) were performed on a Zeiss SmartEDX elemental analyzer. Transmission electron microscopy (TEM) was performed using a Tecnai G2 F20 S-TWIN TMP transmission electron microscope. The dry polymers for TEM examination were milled, suspended in acetone, and deposited on a Cu specimen grid supported by a holey carbon film.

The surface electron state of the sample was measured using Thermo Scientific K-Alpha X-ray photoelectron spectra (XPS). Photoreduction of Ag ions were carried out using a 300 W Xenon Lamp as a light source. The UV–vis absorption spectra were recorded via a UV-2700 spectrophotometer (Shimadzu Corporation, Japan). The thermal gravimetric analysis (TGA) of the polymer networks were evaluated using a TGA5500 thermogravimetric analyzer over the temperature range 30 to 800 °C under a nitrogen atmosphere with a heating rate of 10 °C/min. Ag was determined using a Aglient 5110 inductively coupled plasma optical emission spectrometer (ICP-OES) or Agilent 7700 inductively coupled plasma mass spectrometry (ICP-MS).

2.6. Catalytic experiments and continuous flow hydrogenation

The catalytic activity of Ag@CMP was tested by reduction reaction of 4-nitrophenol into 4-aminophenol (4-AP) in the presence of sodium borohydride (200 ~ 1000 equivalent to n-NP). In a typical reaction, 0.0757 ~ 0.3783 g of $NaBH_4$ was added into 50 mL 4-NP (0.2 mM) and stirred for a moment until the solution changes from light yellow to bright yellow. Then, 8.4 mg of Ag@CMP (Ag@HCMP-bpybph or Ag@CMP-bpy) was added into the mixture, the reaction started. To monitor the reaction progress, 1 mL of samples was withdrawn at specific intervals time, followed by a filtration with 0.45 μm membrane filter to remove the catalyst. The absorbance of samples was measured on a UV vis spectrometer. In order to further confirm the catalytic activity of Ag@CMP, the catalytic hydrogenation of and methyl orange (MO) was also conducted under the same conditions. After the hydrogenation, the mixture was centrifuged to recover the Ag@CMP nanocatalyst. Successive recycling reactions were carried out to test the reusability of the nanocatalyst. Between every two successive reactions, Ag@CMP nanocatalyst was recovered by repeated centrifugation and washing with ultrapure water very carefully to avoid the catalyst loss, and the recovered nanocatalyst was dried in vacuum at 50 ℃ for 12 h for the next cycling reused. Rate constants (k) were calculated using following equation (1):

$$\ln A/A_0 = \ln c_t/c_0 = -kt + C \quad (1)$$

where A, c, t, and C are molar absorption coefficient, 4-NP concentration, reaction time and constant, respectively.

Continuous flow catalytic tests were carried out at room temperature. Ag@CMPA-bph was cut into a uniform cylinder and put into the syringe, with an effective area of 1.3 cm^2. In the experiment, a syringe was used as a driving device to force 4-NP (0.2 mM mL^{-1}) and $NaBH_4$ (200 equivalent to 4-NP) aqueous solutions through the aerogel material at a flow velocity of 3 ~ 5 mL min^{-1}. The original and filtered solution samples were collected for qualitative analysis. The initial aerogels and the aerogels after catalytic inactivation were collected for infrared analysis to preliminarily infer the catalyst inactivation mechanism.

3. Results and discussion

The synthetic pathway and functionalization of CMP materials are shown in Fig. 1, including synthesis of CMPs, post-synthesis

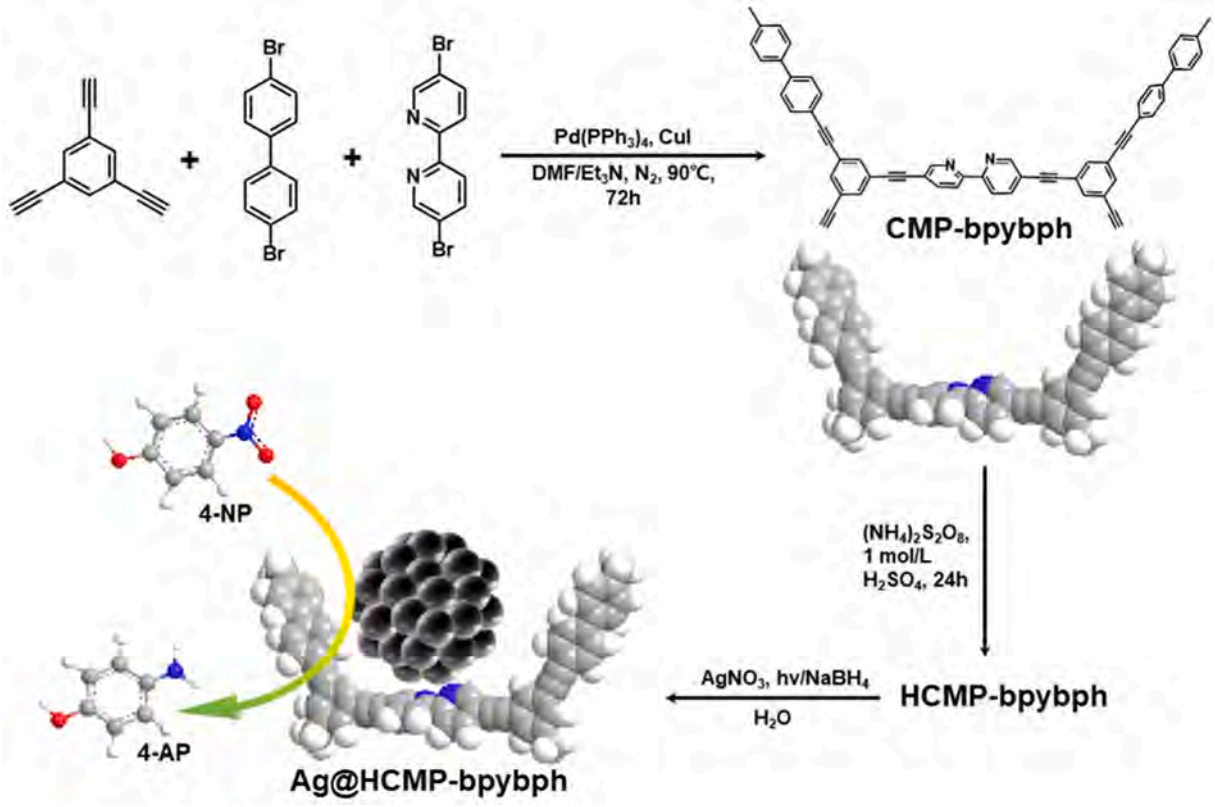

Fig. 1. Illustration of the synthesis route and molecular structure of HCMP-bpy for support of Ag NPs. C, light gray; N, blue; H, white; Ag NPs, dark gray. (For interpretation of the references to color in this figure legend, the reader is referred to the web version of this article.)

modification of the CMP, loading of Ag nanoparticles (NPs) and catalytic performance testing. In the following sections, we first discuss the synthesis and morphology control of CMP as well as the loading of Ag nanocatalyst. The pyridine functional group in CMP network is beneficial to collect Ag ions and anchor Ag NPs [51–53], so that the Ag NPs are evenly distributed in the whole CMP substrate. Compared with the $NaBH_4$ reduction method, the photoreduction method is indeed more conducive to the preparation of more uniform Ag NPs. The synthesized Ag@CMP composite catalyst shows excellent catalytic performance in the treatment of wastewater containing 4-NP or azo dyes. Meanwhile, we confirmed the feasibility of adjusting the morphology of CMP substrates by adjusting the reaction solvent, monomer type and proportion. At last, we simulate the whole system to treat 4-NP wastewater in continuous flow state.

3.1. Design considerations of CMPs

In this work, the CMP networks were synthesized by Sonogashira–Hagihara cross-coupling with 1,3,5-Triethynylbenzene as the core and 5,5′-Dibromo-2,2′-bipyridyl and/or 4,4′-Dibromobiphenyl as the links (Fig. 1). The pyridine groups in CMP networks can provide an anchor position for Ag ions [51–53], which is beneficial to the subsequent in-situ reduction of Ag ions and growth of Ag NPs. Using DMF as the solvent and triethylamine as the acid binding agent, when the ratio of alkynyl and bromine functional groups is 1:2, the obtained CMP, CMP-bpybph, which is almost entirely composed of nano-spherical particles with rough surface (Fig. 2a), insoluble in ordinary organic solvents and water.

3.2. Post-synthesis modification of CMP

Since CMPs are essentially composed of aromatic rings and carbon–carbon triple bonds and the surface of CMPs is relatively rough on the microscopic level, the properties of most CMPs are superhydrophobic [54]. As a result, some CMPs are difficult to be completely wetted by water, thus obstructing the contact between contaminants in water and the catalytic active site. To promote the application of water treatment, the water wettability of the material can be improved by post-synthesis modification [55–57]. Usually, the wettability of CMP networks can be changed by introducing monomers with hydrophilic functional groups [58]. Furthermore, the surface wettability of the material can be changed more easily by oxidizing the material with 1 mol/L H_2SO_4 solution saturated with $(NH_4)_2S_2O_8$ [59]. Therefore, in this work, we used chemical modification [50] to improve the wettability of CMP-bpybph.

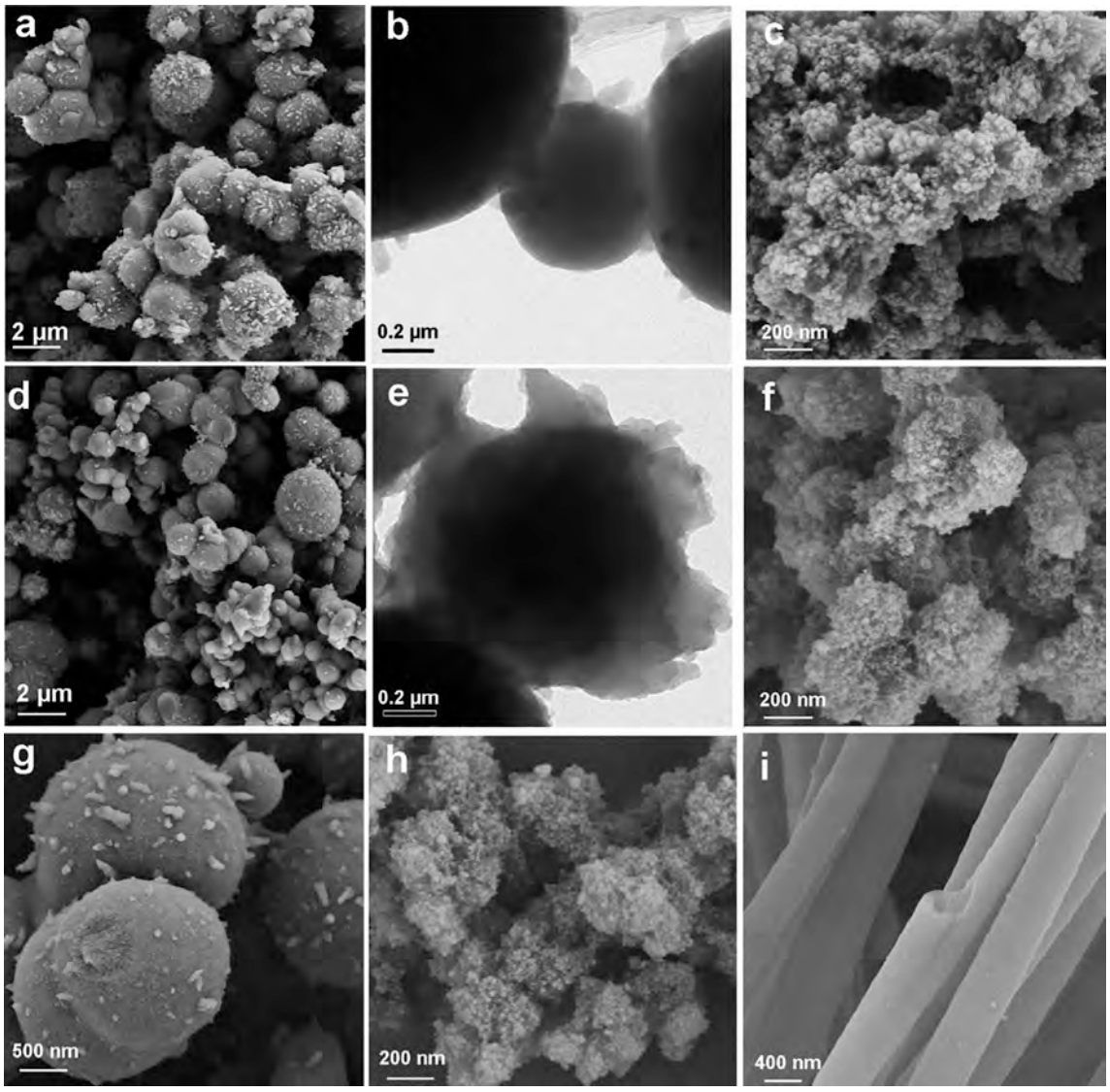

Fig. 2. Morphological control. SEM image (a) and TEM image (b) of CMP-bpybph; SEM image (d) and TEM image (e) of HCMP-bpybph; SEM image of CMP-bpy (c) and Ag@CMP-bpy (f); SEM image of Ag@HCMP-bpybph (g), Ag@CMP-bpy (h), Ag@CMPA-bph (i).

Compared to CMP-bpybph with a water contact angle (CA) of 94.25°, the hydrophilicity of HCMP-bpybph with a CA of 78.32° was improved after chemical modification (Fig. S1). Meanwhile, the SEM image (Fig. 2a) and TEM image (Fig. 2b) of CMP-bpybph before hydrophilic modification and the SEM image (Fig. 2d) and TEM image (Fig. 2e) of HCMP-bpybph after hydrophilic modification showed the chemical hydrophilic modification did not change the morphology and microstructure of the substrate materials. Meanwhile, the SEM image of CMP-bpy (Fig. 2c) and Ag@CMP-bpy (Fig. 2f) showed that metal loading did not affect the microstructure of the materials. These results further verified the chemical stability of CMP substrate materials.

3.3. Morphological control for CMP

To further improve the catalytic stability and recoverability of the catalyst, the morphology of CMP substrates was regulated. Previous studies show the regulation of reaction conditions, monomer types and monomer mole ratio can fundamentally control the microscopic morphology and macroscopic structure of CMP substrates [60–62]. We further confirm that the molar ratio of alkyne and bromine functional groups in the polymerization process has an important effect on the morphology of the CMP networks. We found that when the molar ratio of alkyne and bromine functional groups was 1:2, the obtained Ag@HCMP-bpybph presented nano-spherical structure (Fig. 2g). However, when the molar ratio of alkyne and bromine functional groups was adjusted to 2:1, the synthesized Ag@CMP-bpy was mainly composed of amorphous nanoclusters (Fig. 2h and Fig. S2a), and when the molar ratio of alkyne and bromine functional groups was adjusted to 3:1, the synthesized Ag@CMP-bpy was mainly composed of nanotube structure (Fig. S2b).

The pore size distribution of CMP-bpy and CMP-bpybph was calculated by Barrett–Joyner–Hallender (BJH) method. The nitrogen sorption isotherm for CMP-bpybph substrate was shown in Fig. S3a, the Brunauer-Emmet-Teller (BET) specific surface area of CMP-bpybph was 16.61 $m^2\ g^{-1}$, which is unusual for CMP [63]. This indicates that the alkynyl molar ratio regulates the porosity of CMPs. When the molar ratio of alkyne and bromine functional groups is adjusted to 1:2, the microstructure of CMP-bpybph material is mainly composed of nanoparticles, resulting in the low porosity of CMP-bpybph material. The nitrogen sorption isotherm for CMP-bpy substrate was shown in Fig. S3b, the BET specific surface area of CMP-bpy was 586.31 $m^2\ g^{-1}$, and the average pore size of CMP-bpy was 6.11 nm with micropores and mesoporous channels as the main channels.

Besides, the monomer type also has an important influence on the morphology of the obtained CMP networks. When the molar ratio of alkyne and bromine functional groups was fixed at 2:1, compared with Ag@CMP-bpy, the bipyridyl monomer in Ag@CMPA-bph was replaced by biphenyl monomer, which promotes the formation of internal nanotube structure (Fig. 2i). Presently, systematic experimental and/or theoretical explanations of these adjustable factors and the resulting differences in special morphology caused by this are missing. Therefore, in the future work, to elucidate the regulation mechanism of CMPs theoretically through experiments and/or theoretical simulation and exploring the internal structure–activity relationship between molecular structure and final product is crucial to synthesize CMP substrate materials further accurately.

3.4. Ag nanocatalyst supported by CMPs

For heterogeneous water treatment, the ideal feature of nanocatalysts is that the active sites are uniformly dispersed over loose distances in the substrate material. Structural illustration of Ag@CMP is shown in Fig. 3a. The morphology and particle size of Ag NPs in Ag@HCMP-bpybph were studied by transmission electron microscopy (TEM). The average diameter of Ag NPs was about 4.12 nm, and they were uniformly dispersed in HCMP-bpybph substrate (Fig. 3b). The inductively coupled plasma optical emission spectrometer (ICP-OES) result indicated that the Ag load of Ag@HCMP-bpybph-10 was about 12.65 wt%. High-resolution TEM images (HR-TEM, Fig. 3c) confirmed that the Ag NPs were in crystalline phase with a crystal plane spacing of

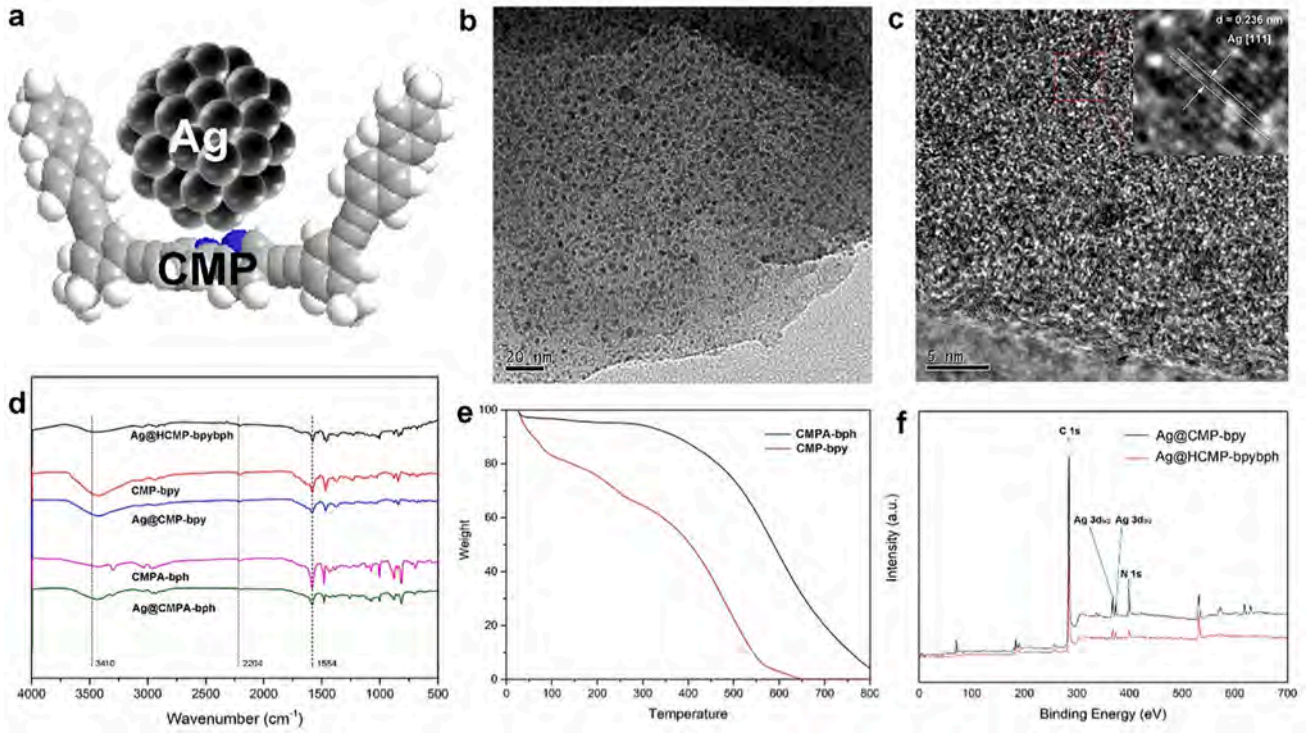

Fig. 3. Materials Characterization. (a) Structural illustration of Ag@CMP. TEM image of Ag@HCMP-bpybph showing the uniform distribution (b) and the crystalline phase (c) of Ag NPs. (d) FTIR spectra of all materials. (e) TGA of CMPA-bph and CMP-bpy. (f) XPS of Ag@CMP-bpy and Ag@HCMP-bpybph.

0.236 nm, which corresponds to the Ag NPs [1 1 1] lattice plane.

The structure of the CMPs was investigated by the solid-state ^{13}C CP/MAS NMR spectra. As shown in Fig. S4, for CMP-bpy, the peaks at ca. 81.4, 92.1, and 123.1 ppm are assigned to terminal alkyne, C_{Ar}-C≡C-C_{Ar}, and C_{Ar}-C≡C-, respectively. Meanwhile, the three resonances at ca. 153.2, 138.1, and 120.9 ppm owing to the ortho-, para- and meta-substituted carbon of the pyridine unit [38]. As for CMPA-bph, the peaks at ca. 90.0, 123.3 and 131.6 ppm are assigned to C_{Ar}-C≡C-C_{Ar}, C_{Ar}-C≡C-, and C_{Ar}-H, respectively. The resonance peaks at ca. 127.6 and 139.1 ppm owing to the non-substituted and substituted aromatic carbon on biphenyl, respectively [48].

The FT-IR was used to further characterize the prepared materials (Fig. 3d). The strong absorption peak observed near 3410 cm^{-1} was the stretching vibration peak of -C≡CH. The absorption peak observed near 2204 cm^{-1} was a stretching vibration peak of -C≡C-. As well as the presence of benzene and pyridine rings was confirmed by the observation of strong stretching vibration bands near 1584 cm^{-1}. In the Raman spectra (Fig. S5), the Raman spectra of CMP-bpy display a peak at 2188.4 cm^{-1} attributed to the vibration of conjugated diyne links [64]. The Raman spectra of CMP-bpy and CMP-bph display a peak at ca. 1600 and 1350 cm^{-1} belonging to the in-phase stretching vibration of sp^2 carbon lattice in aromatic rings (G bands) and the breathing vibration of sp^2 carbon domains in aromatic rings (D bands), respectively [65]. These results indicate the formation of the extended π-conjugated skeleton among the polymers.

The thermogravimetric curve (TG, Fig. 3e) shows that CMPA-bph has higher thermal stability than CMP-bpy, which may be caused by the relatively high crosslinking degree of CMPA-bph. TG was performed to test the thermal stabilities and the successful loading of Ag of the Ag@CMP-bpy (Fig. S6) and Ag@CMPA-bph (Fig. S7). The amorphous structure of CMPs (Fig. S8) and crystallinity of Ag@CMPs (Fig. S9) were identified by PXRD analysis. As shown in Fig. S9, the existing five reflections located at 2θ values of 38.3°, 44.5°, 64.6°, 77.6°, and 81.7° could be assigned to the (1 1 1), (2 0 0), (2 2 0), (3 1 1), and (2 2 2) planes of face-centered cubic (fcc) phase of silver [66]. The X-ray photoelectron spectroscopy (XPS) further showed the presence of Ag NPs in the composites, and the characteristics of Ag species were observed at binding energies of 368 eV ($3d_{5/2}$) and 374 eV ($3d_{3/2}$), respectively (Fig. 3f, Fig. S10, and Fig. S11). These results confirm the successful preparation of organic synthetic CMP substrates and Ag@CMP composite materials.

The dispersion and particle size distribution of Ag NPs in CMP substrate was further studied by TEM and particle size analysis. Due to the enhanced interaction between the pyridine group and Ag ions, the Ag ions are usually enriched around the pyridine group [51–53], which makes the reduced Ag NPs evenly dispersed in the CMP substrate and prevents the aggregation of Ag NPs, thus forming finer Ag NPs. As shown in Fig. S12, the Ag element is uniformly dispersed on the CMP-bpy substance with pyridine group, while the Ag element is relatively concentrated on the surface of the CMPA-bph substance without the pyridine group. Furthermore, the average particle sizes of Ag NPs in Ag@CMP-bpy-1, Ag@HCMP-bpybph-10, and Ag@CMP-bpy-0.1 are 7.16 nm, 4.12 nm, and 1.92 nm, respectively (Fig. 4). EDX mapping of Ag@HCMP-bpybph (Fig. S13 and Table S1) and Ag@CMP-bpy (Fig. S14, Fig. S15, and Table S2) also confirmed the presence of Ag NPs, which were uniformly distributed in the CMP substrate. The results of ICP-OES confirmed that the Ag loading of Ag@HCMP-bpybph-10, Ag@CMP-bpy-1, and Ag@CMP-bpy-0.1 were about 12.65 wt%, 2.98 wt%, and 0.062 wt%, respectively.

To our surprise, compared with Ag@CMP-bpy-1 obtained by $NaBH_4$ reduction, Ag@CMP-bpy-1 obtained by photoreduction formed finer Ag NPs with a narrower and more uniform particle size distribution (Fig. S16). We assume that the growth of metal NPs (MNPs) in substrate mainly includes uniform diffusion of metal precursor and reduction of metal ions. In the $NaBH_4$ reduction process [44], after $NaBH_4$ is added to an aqueous solution, BH^{4-} species, as a reducing agent, can rapidly react with free metal ions in the solvent and rapidly form metal core. The newly formed metal core is not fixed and has high surface energy, causing agglomeration to form larger Ag NPs. Conversely, in photoreduction process [42], reducing agent is a kind of active substance produced under light induction. These substances are produced throughout

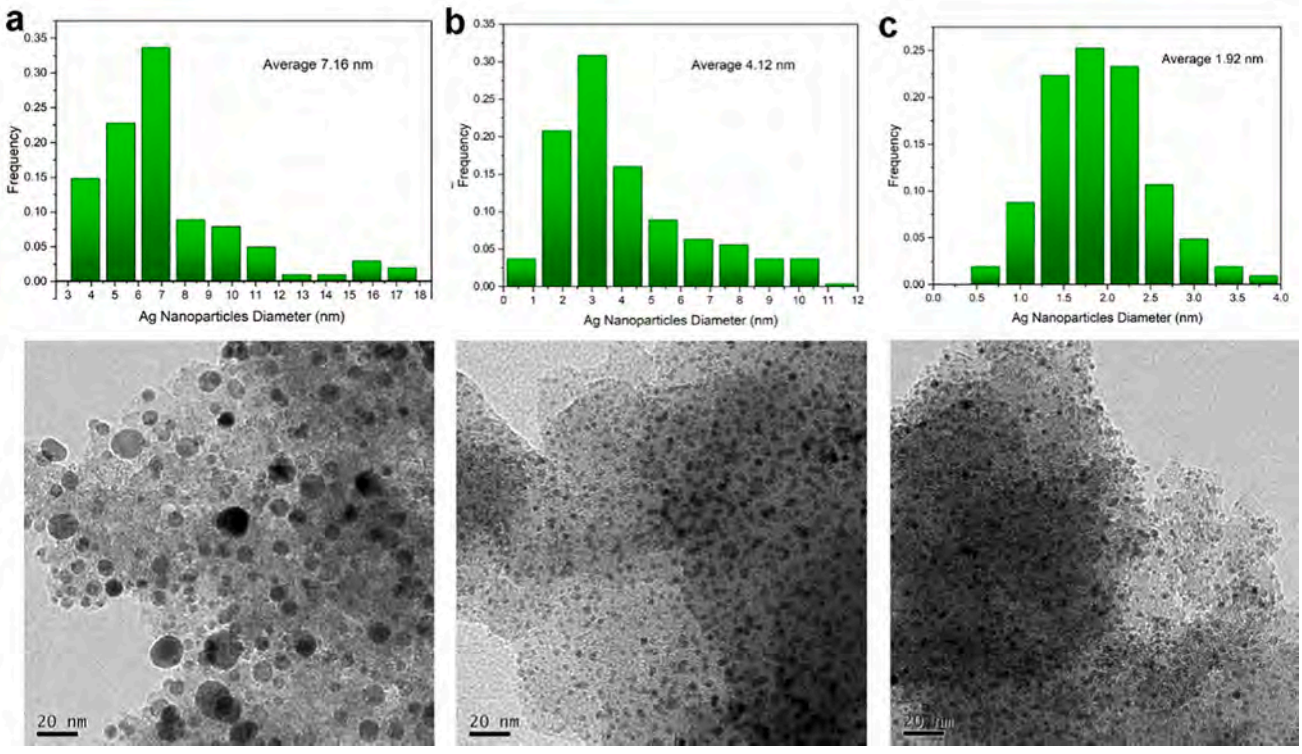

Fig. 4. Particle size analysis of Ag NPs. TEM images and size distribution of Ag NPs (statistical data for over 100 NPs) of (a) Ag@CMP-bpy-1, (b) Ag@HCMP-bpybph-10, and (c) Ag@CMP-bpy-0.1. 10, 1, and 0.1 represent the concentrations of metal precursors.

the solvent system to ensure that the reduction process occurs simultaneously and at a gentle and steady rate, resulting in the formation of finer particles, narrower particle size distributions, and more uniform dispersion distances. Therefore, we believe that photoreduction [42,67,68] is a simple and effective method to prepare ultrafine MNPs.

3.5. Catalytic activity and reusability of Ag@CMP

To estimate the catalytic performance of the Ag@CMP composites, the catalytic removal of 4-nitrophenol (4-NP) and/or methyl orange (MO) in water was used as the application model. Taking 4-NP as an example, according to the Langmuir-Hinshelwood mechanism of 4-NP catalytic reduction [6,42,44], the removal process is as follows: $NaBH_4$ reacts with water to form large quantities of BH^{4-} ions. The Ag@CMP as a catalyst is added to the 4-NP solution, wherein Ag NPs help BH^{4-} dissociation H• free radicals. 4-NP molecules near the catalyst are adsorbed into the porous structure of the catalyst, and the H• free radicals were used to attack the N^+ of the nitro group in 4-NP and catalyze the hydrogenation reduction of 4-NP to 4-AP. The reduction product 4-AP is released from the hydrophobic channels of the catalyst, and Ag NPs within the catalyst is exposed and can continue to react with the remaining 4-NP. During the reaction process, samples were taken and filtered at a certain time interval and determined by ultraviolet spectrophotometry.

In the presence of Ag@HCMP-bpybph, the intensity of the absorption peak (characteristic peak of 4-NP) at 400 nm disappeared at about 3 min, and formed at 300 nm (characteristic peak of 4-AP), indicating that the system can catalytically reduce 4-NP to 4-AP in a relatively short time (Fig. 5a). The reactions were considered as pseudo-first-order reactions and the apparent rate constant value was calculated from the slope of the plot $\ln(c_t/c_0)$ against time to be $-0.01544\ s^{-1}$ (Fig. 5b). Fig. S17 shows that the molecular structure of Ag@HCMP-bpybph after five consecutive catalytic cycles is destroyed, resulting in deactivation of the catalyst.

Conspicuously, Ag@CMP-bpy reaction system can not only catalyze the reduction of 4-NP in about 5 min (Fig. 5c and Fig. S18a) with the slope of the plot $\ln(c_t/c_0)$ against time to be $-0.01238\ s^{-1}$ (Fig. S18b) but also maintained high efficiency in 11 cycles of catalysis (Fig. S19). This indicates that the system not only has high catalytic activity but also has outstanding catalytic stability. Comparative tests were conducted for suggesting Ag@CMPs paly an indispensable role in the reduction reaction. In the absence of $NaBH_4$, when Ag@CMPs was added to the 4-NP solution, the absorption peak intensity of the sample at 317 nm decreased slightly, but no new peak was generated after 30 min (Fig. S18c), indicating that the decrease of 4-NP at the UV–vis absorption peak at 317 nm could be caused by the adsorption of the catalyst. In the absence of catalyst, the intensity of the UV absorption peak at 400 nm of the sample did not decrease with time within 30 min (Fig. S18d and Fig. S20a), indicating that the hydrogenation reduction reaction basically stagnated.

In addition, the catalytic performance of CMP-bpy was tested, as shown in Fig. S20b, after adding NaBH4 to 4-NP, the UV absorption peak of the mixed solution changed from 317 nm to 400 nm. Then CMP-bpy was added, the absorption peak of the sample at 400 nm changed slightly due to the adsorption and desorption of CMP-bpy. However, after 30 min, there was still no new peak appears at 298 nm corresponding to product 4-AP, indicating that the residual Pd and Cu in CMP-bpy do not play a role in the catalytic process. The stability of the catalyst was also confirmed by FT-IR before and after the catalysis (Fig. S21). Meanwhile, TEM and EDX mapping images showed that the distribution of Ag NPs also remained uniform and stable (Fig. S15, Fresh Ag@CMP-bpy; Fig. S22, Ag@CMP-bpy after 11 cycles). Table S3

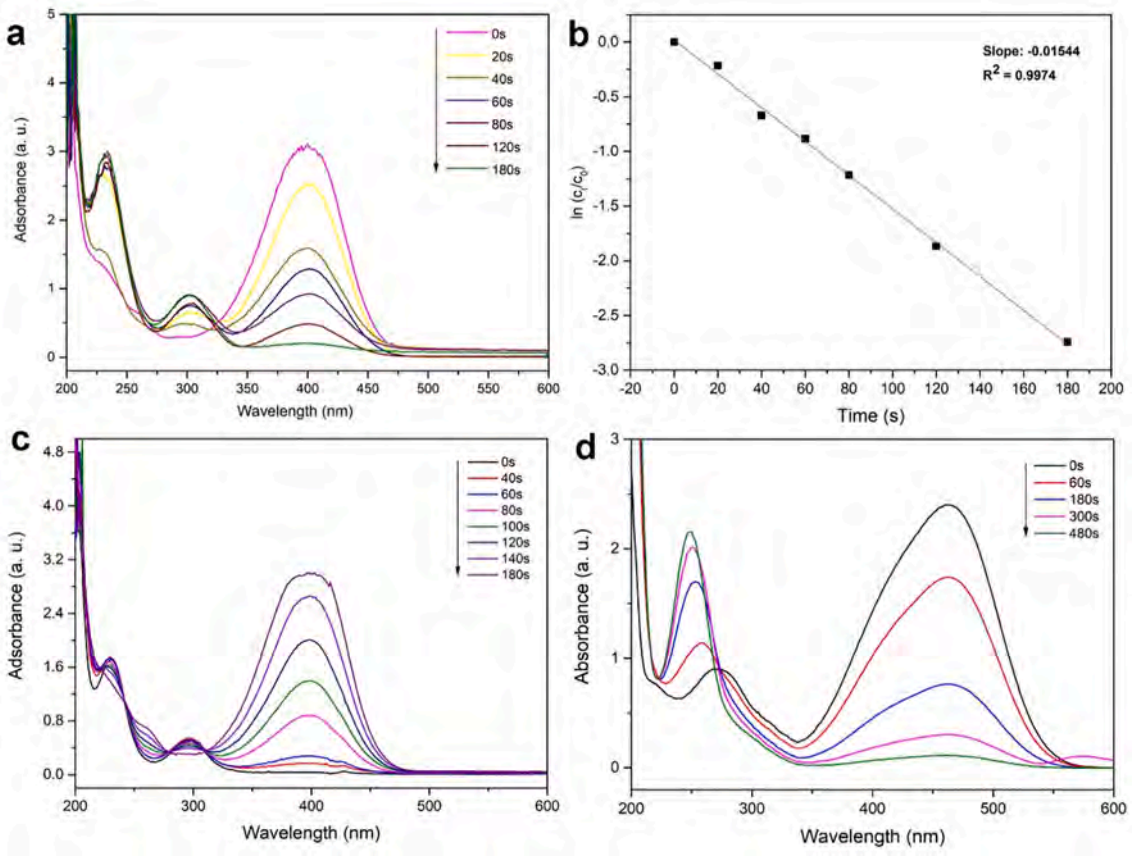

Fig. 5. Catalytic activity and degradation products. Time-dependent UV–vis absorption spectra (a) and plots of ln (c_t/c_0) versus time (b) of the hydrogenation of 4-NP catalyzed by Ag@HCMP-bpybph; Time-dependent UV–vis absorption spectra of the hydrogenation of 4-NP (c) and MO (d) catalyzed by Ag@CMP-bpy.

compared the catalytic activity of Ag@CMP-bpy and other reported similar catalysts. In addition, in the presence of Ag@CMP-bpy, the absorption peak (characteristic peak of MO) at 465 nm gradually weakened with the advance of reaction time, and MO could be degraded in about 10 min (Fig. 5d). This further indicates that the Ag@CMP-bpy system has high catalytic hydrogenation activity.

To investigate the process potential of Ag@CMP-bpy nanocatalysts in the treatment of real samples, hydrogenation of 4-NP loading on distilled water, tap water, and river water was proposed. When a certain amount of 4-NP is added to tap water and river water, the solution immediately appears bright yellow, while the deionized water and bottled water containing 4-NP appear pale yellow. As shown in Fig. S23a, in the absence of $NaBH_4$, UV–vis spectra of different water samples were detected and no peaks were found at 298 nm, indicating that no substances in these water samples capable of initiating the hydrogenation reaction and acting as $NaBH_4$. The concentration of 4-NP was adjusted to 0.2 mM, compared with other water samples (Fig. S23a), the river water containing 4-NP had the weakest UV absorption peak at 400 nm (Fig. S24a). As shown in Fig. S23c-k, the reaction was complete within 5 min after $NaBH_4$ and Ag@CMP-bpy were added to tap water containing 4-NP. Meanwhile, Ag@CMP-bpy nanocatalyst also showed the process potential in river water samples (Fig. S24b, c), the reaction was complete within 4 min after $NaBH_4$ and Ag@CMP-bpy were added to river water containing 4-NP.

To detect whether the material pollutes the environment, we detect the leaching of Ag in the reduced water sample. The reduced water sample was determined using Agilent 7700 inductively coupled plasma mass spectrometry (ICP-MS). The concentration of Ag in the water sample were calculated using following equation (2):

$$C_1 = C_0 * f \quad (2)$$

where C_1, C_0, and f are concentration of Ag element in sample stock (mg/L), concentration of Ag elements in the test solution (mg/L), and dilution ratio, respectively. The concentration of Ag element in the samples was 6.1 μg/L. For biocompatibility [69–71], the leaching of trace Ag elements could pollute the environment and harm the health of aquatic organisms.

3.6. Flow-through catalytic performance of Ag@CMPA

The outstanding catalytic performance of Ag@CMP composites encourages us to further explore their application level in continuous flow state [72–74]. We prepared CMPA-bph hydrogel by morphology control strategy (Fig. 6a), and obtained CMPA-bph aerogel after vacuum drying (Fig. 6b). Compared to CMPA-bph hydrogel, CMPA-bph aerogel is brown-yellow in color and slightly reduced in size, which may help to resist polymer chain shrinkage and prevent structural collapse [75]. Interestingly, the resulting CMPA-bph can return to its original shape after loading (Fig. 6c) and loading removal (Fig. 6d), showing its good elasticity. We further prepared Ag@CMPA-bph aerogel (Fig. S25), and ICP-OES results confirmed that the Ag loading of Ag@CMPA-bph was about 0.086 wt%. The EDX mapping of Ag@CMPA-bph (Fig. S26, Fig. S27, and Table S4) further confirmed that the Ag NPs were uniformly distributed in the CMPA-bph substrate.

A proof-of-concept wastewater treatment system is shown in Fig. 6f, mainly includes five steps: (1) The industrial wastewater is pretreated to meet the feed requirements ($\leq$70 mg L^{-1}) of the subsequent treatment unit; (2) For the dosing pool, under the electrical drive, $NaBH_4$ enters the dosing pool and mixes with feed wastewater to generate active substances and start the reaction; (3) The mixed solution enters the reaction channel at a flow rate of 5 mL min^{-1} and fully reacts; (4) The fully reacted mixture enters the slow-flow tank. The catalyst flowing out is

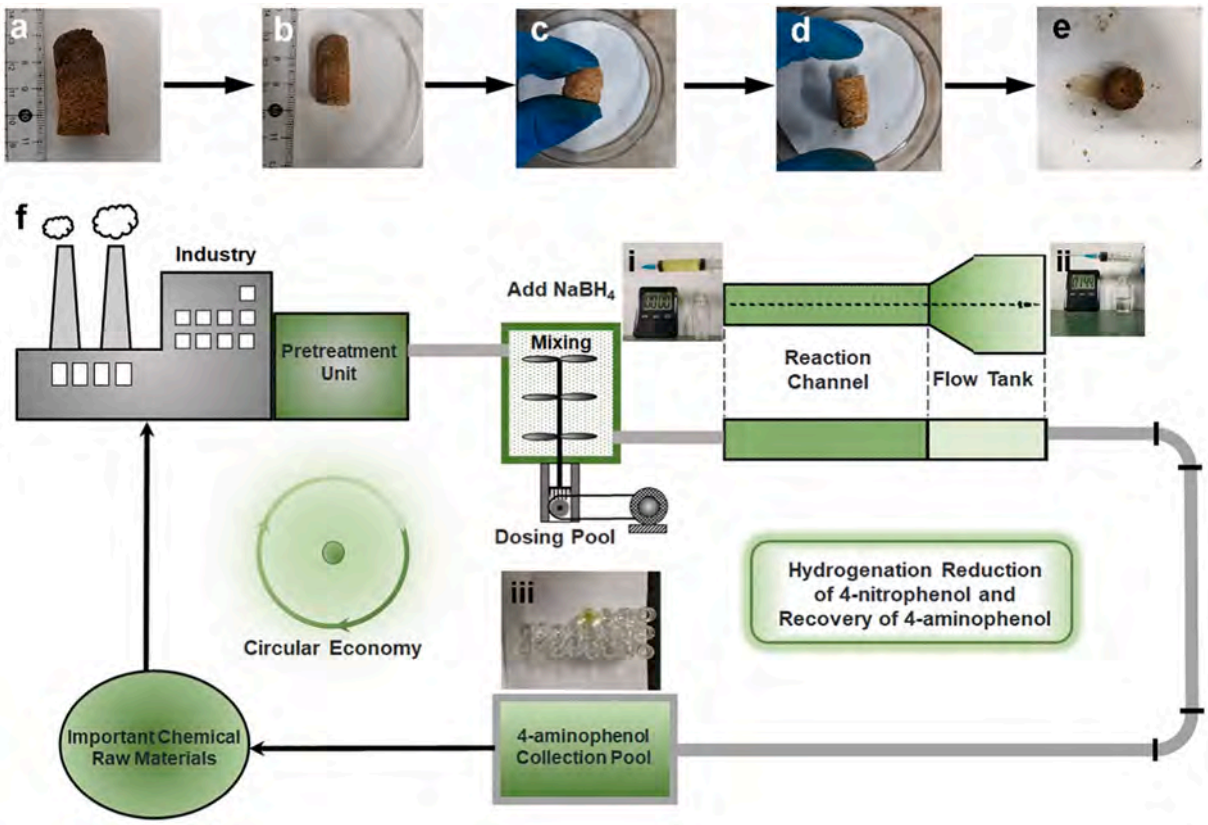

Fig. 6. Processable Ag@CMP aerogel material and schematic diagram of wastewater treatment and circulation system. Camera photos of CMPA-bph hydrogel (a) and CMPA-bph aerogel (b). Images of Ag@CMPA-bph under loaded (c) and unloaded (d) conditions. (e) Camera photos of the collapsing Ag@CMPA-bph material. (f) the system includes the dosing pool, the reaction device, *p*-nitrophenol collection tank, and the catalyst recovery device.

recycled and reused, and the raffinate enters the collection tank; (5) The important chemical raw materials in the raffinate are recovered and qualified wastewater is discharged into the environment. The reaction device and the catalyst recovery device are the core of the wastewater treatment system.

The specific experimental device is shown in Fig. S28. At room temperature, a syringe-driven filter container was used for a continuous flow catalytic test. In general, the removal efficiency of pollutants depends on the residence time of reactants [76–78]. The permeation experiment showed that the treatment system achieves an outstanding permeation flux of 1603 L $m^{-2}h^{-1}$ (LMH) with more than 99% 4-NP reduction efficiency. Meanwhile, the catalyst could maintain catalytic stability in the continuous flow process, and FT-IR spectra (Fig. S29) before and after the catalysis showed that the molecular structure of the catalyst remains stable. However, the catalyst was inactivated in the subsequent application, which could be caused by the destruction of the macroscopic structure (Fig. 6e) of the catalyst by pressure.

4. Conclusions

In this work, we propose feasible solutions to two basic challenges of noble metal nanocatalysts for catalytic hydrogenation reduction of 4-NP in water: catalyst fixation and fine synthesis. Firstly, we improved the existing bipyridine-based CMPs by post-synthesis modification and morphology adjustment, demonstrating the technical potential of CMPs as material substrates. The porous properties, physical and chemical stability, and design flexibility of CMPs are keys to the stable support of noble metal catalysts. Subsequently, we prepared a composite catalyst with ultrafine Ag NPs (average particle size: 1.92 nm) by anchoring of bipyridine group in CMP networks and photoreduction method, which demonstrated high activity and stability (more than ten cycles) for the reduction of 4-NP. We synthesized a processable Ag@CMPA-bph aerogel for reduction of 4-NP in water under continuous flow, which achieves high permeation flux (1603 LMH) with high reduction efficiency (over 99%). This work demonstrates the potential of design and regulation based on existing CMP families to provide support for the fine synthesis of noble metal catalysts. We believe that this work will further advance the gelation of CMP materials and the refinement of noble metal catalysts to extend their sustainable applications in the environmental and energy fields.

Declaration of Competing Interest

The authors declare that they have no known competing financial interests or personal relationships that could have appeared to influence the work reported in this paper.

Acknowledgments

The study was financially supported by the Program for Changjiang Scholars and Innovative Research Team in University (IRT-13R17), the National Natural Science Foundation of China (82003363, U20A20323, 52100181, 51521006, 51378190, 51979103, 51679085, 51308200), the Fundamental Research Funds for the Central Universities of China (531107051205), the Funds of Hunan Science and Technology Innovation Project (2018RS3115), Natural Science Foundation of Hunan Province, China (S2021JJQNJJ2330, S2020JJ5069), the Key Research and Development Project of Hunan Province of China (2017SK2241), the Changsha Municipal Natural Science Foundation (kq2007059) and the Project funded by China Postdoctoral Science Foundation (2021T140192, 2021M690054).

Appendix A. Supplementary data

Supplementary data to this article can be found online at https://doi.org/10.1016/j.cej.2022.136207.

References

[1] B. Lai, Z. Chen, Y. Zhou, P. Yang, J. Wang, Z. Chen, Removal of high concentration p-nitrophenol in aqueous solution by zero valent iron with ultrasonic irradiation (US–ZVI), J. Hazard. Mater. 250–251 (2013) 220–228.
[2] B. Lai, Y.-H. Zhang, R. Li, Y.-X. Zhou, J. Wang, Influence of operating temperature on the reduction of high concentration p-nitrophenol (PNP) by zero valent iron (ZVI), Chem. Eng. J. 249 (2014) 143–152.
[3] Y. Ren, J. Li, L. Lai, B. Lai, Premagnetization enhancing the reactivity of Fe0/(passivated Fe0) system for high concentration p-nitrophenol removal in aqueous solution, Chemosphere 194 (2018) 634–643.
[4] Y. Fu, L. Qin, D. Huang, G. Zeng, C. Lai, B. Li, J. He, H. Yi, M. Zhang, M. Cheng, X. Wen, Chitosan functionalized activated coke for Au nanoparticles anchoring: Green synthesis and catalytic activities in hydrogenation of nitrophenols and azo dyes, Appl. Catal. B 255 (2019), 117740.
[5] L. Qin, H. Yi, G. Zeng, C. Lai, D. Huang, P. Xu, Y. Fu, J. He, B. Li, C. Zhang, M. Cheng, H. Wang, X. Liu, Hierarchical porous carbon material restricted Au catalyst for highly catalytic reduction of nitroaromatics, J. Hazard. Mater. 380 (2019), 120864.
[6] L. Qin, Z. Zeng, G. Zeng, C. Lai, A. Duan, R. Xiao, D. Huang, Y. Fu, H. Yi, B. Li, X. Liu, S. Liu, M. Zhang, D. Jiang, Cooperative catalytic performance of bimetallic Ni-Au nanocatalyst for highly efficient hydrogenation of nitroaromatics and corresponding mechanism insight, Appl. Catal. B 259 (2019), 118035.
[7] D. Wang, D. Astruc, The golden age of transfer hydrogenation, Chem. Rev. 115 (13) (2015) 6621–6686.
[8] S. Zhang, C.-R. Chang, Z.-Q. Huang, J. Li, Z. Wu, Y. Ma, Z. Zhang, Y. Wang, Y. Qu, High catalytic activity and chemoselectivity of sub-nanometric Pd clusters on porous nanorods of CeO2 for hydrogenation of nitroarenes, J. Am. Chem. Soc. 138 (8) (2016) 2629–2637.
[9] J. Xia, G. He, L. Zhang, X. Sun, X. Wang, Hydrogenation of nitrophenols catalyzed by carbon black-supported nickel nanoparticles under mild conditions, Appl. Catal. B 180 (2016) 408–415.
[10] Z. Dong, X. Le, X. Li, W. Zhang, C. Dong, J. Ma, Silver nanoparticles immobilized on fibrous nano-silica as highly efficient and recyclable heterogeneous catalyst for reduction of 4-nitrophenol and 2-nitroaniline, Appl. Catal. B 158–159 (2014) 129–135.
[11] J.G. Kim, M.C. Cha, J. Lee, T. Choi, J.Y. Chang, Preparation of a sulfur-functionalized microporous polymer sponge and in situ growth of silver nanoparticles: A compressible monolithic catalyst, ACS Appl. Mater. Inter. 9 (43) (2017) 38081–38088.
[12] L. Tan, B. Tan, Functionalized hierarchical porous polymeric monoliths as versatile platforms to support uniform and ultrafine metal nanoparticles for heterogeneous catalysis, Chem. Eng. J. 390 (2020), 124485.
[13] B. Qiao, A. Wang, X. Yang, L.F. Allard, Z. Jiang, Y. Cui, J. Liu, J. Li, T. Zhang, Single-atom catalysis of CO oxidation using Pt1/FeOx, Nat. Chem. 3 (8) (2011) 634–641.
[14] L. Liu, A. Corma, Metal catalysts for heterogeneous catalysis: From single atoms to nanoclusters and nanoparticles, Chem. Rev. 118 (2018) 4981–5079.
[15] L. Lin, S. Yao, R. Gao, X. Liang, Q. Yu, Y. Deng, J. Liu, M.i. Peng, Z. Jiang, S. Li, Y.-W. Li, X.-D. Wen, W.u. Zhou, D. Ma, A highly CO-tolerant atomically dispersed Pt catalyst for chemoselective hydrogenation, Nat. Nanotechnol. 14 (4) (2019) 354–361.
[16] T.W. van Deelen, C. Hernández Mejía, K.P. de Jong, Control of metal-support interactions in heterogeneous catalysts to enhance activity and selectivity, Nature, Catalysis 2 (11) (2019) 955–970.
[17] C. Xia, Y. Qiu, Y. Xia, P. Zhu, G. King, X. Zhang, Z. Wu, J.Y. Kim, D.A. Cullen, D. Zheng, P. Li, M. Shakouri, E. Heredia, P. Cui, H.N. Alshareef, Y. Hu, H. Wang, General synthesis of single-atom catalysts with high metal loading using graphene quantum dots, Nat. Chem. 13 (9) (2021) 887–894.
[18] X.-H. Jiang, L.-S. Zhang, H.-Y. Liu, D.-S. Wu, F.-Y. Wu, L. Tian, L.-L. Liu, J.-P. Zou, S.-L. Luo, B.-B. Chen, Silver single atom in carbon nitride catalyst for highly efficient photocatalytic hydrogen evolution, Angew. Chem. Int. Ed. 59 (51) (2020) 23112–23116.
[19] Z. Huang, T. Ban, Y. Zhang, L. Wang, S. Guo, C.-R. Chang, G. Jing, Boosting the thermal stability and catalytic performance by confining Ag single atom sites over antimony-doped tin oxide via atom trapping, Appl. Catal. B 283 (2021), 119625.
[20] Y. Yang, G. Zeng, D. Huang, C. Zhang, D. He, C. Zhou, W. Wang, W. Xiong, B. Song, H. Yi, S. Ye, X. Ren, In situ grown single-atom cobalt on polymeric carbon nitride with bidentate ligand for efficient photocatalytic degradation of refractory antibiotics, Small 16 (2020) 2001634.
[21] S. Wei, A. Li, J.-C. Liu, Z. Li, W. Chen, Y. Gong, Q. Zhang, W.-C. Cheong, Y.u. Wang, L. Zheng, H. Xiao, C. Chen, D. Wang, Q. Peng, L. Gu, X. Han, J. Li, Y. Li, Direct observation of noble metal nanoparticles transforming to thermally stable single atoms, Nat. Nanotechnol. 13 (9) (2018) 856–861.
[22] A. Corma, P. Concepción, M. Boronat, M.J. Sabater, J. Navas, M.J. Yacaman, E. Larios, A. Posadas, M.A. López-Quintela, D. Buceta, E. Mendoza, G. Guilera, A. Mayoral, Exceptional oxidation activity with size-controlled supported gold clusters of low atomicity, Nat. Chem. 5 (9) (2013) 775–781.
[23] X. Liu, J. Iocozzia, Y. Wang, X. Cui, Y. Chen, S. Zhao, Z. Li, Z. Lin, Noble metal-metal oxide nanohybrids with tailored nanostructures for efficient solar energy conversion, photocatalysis and environmental remediation, Energy Environ. Sci. 10 (2) (2017) 402–434.
[24] S. Cheng, X. Pan, C. Zhang, X. Lin, Q. Zhuang, Y. Jiao, W. Dong, X. Qi, UV-assisted ultrafast construction of robust Fe3O4/polydopamine/Ag Fenton-like catalysts for highly efficient micropollutant decomposition, Sci. Total Environ. 810 (2022), 151182.

[25] U.C. Rajesh, Y. Losovyj, C.-H. Chen, J.M. Zaleski, Designing synergistic nanocatalysts for multiple substrate activation: Interlattice Ag–Fe3O4 hybrid materials for CO2-inserted lactones, ACS Catal. 10 (2020) 3349–3359.
[26] X. Zhai, S. Cheng, H. Wang, C. Zhang, Y. Li, W. Dong, Fast preparation of Fe3O4@polydopamine/Au for highly efficient degradation of tetracycline, Chemosphere 285 (2021), 131523.
[27] L. Jiao, H.-L. Jiang, Metal-organic-framework-based single-atom catalysts for energy applications, Chem 5 (4) (2019) 786–804.
[28] W. Zhong, R. Sa, L. Li, Y. He, L. Li, J. Bi, Z. Zhuang, Y. Yu, Z. Zou, A covalent organic framework bearing single ni sites as a synergistic photocatalyst for selective photoreduction of CO2 to CO, J. Am. Chem. Soc. 141 (18) (2019) 7615–7621.
[29] S. Luo, Z. Zeng, G. Zeng, Z. Liu, R. Xiao, M. Chen, L. Tang, W. Tang, C. Lai, M. Cheng, B. Shao, Q. Liang, H. Wang, D. Jiang, Metal organic frameworks as robust host of palladium nanoparticles in heterogeneous catalysis: Synthesis, application, and prospect, ACS Appl. Mater. Inter. 11 (36) (2019) 32579–32598.
[30] Y. Liu, D. Huang, M. Cheng, Z. Liu, C. Lai, C. Zhang, C. Zhou, W. Xiong, L. Qin, B. Shao, Q. Liang, Metal sulfide/MOF-based composites as visible-light-driven photocatalysts for enhanced hydrogen production from water splitting, Coord. Chem. Rev. 409 (2020), 213220.
[31] Y. Liu, H. Cheng, M. Cheng, Z. Liu, D. Huang, G. Zhang, B. Shao, Q. Liang, S. Luo, T. Wu, S. Xiao, The application of zeolitic imidazolate frameworks (ZIFs) and their derivatives based materials for photocatalytic hydrogen evolution and pollutants treatment, Chem. Eng. J. 417 (2021), 127914.
[32] S.-M. Wu, X.-Y. Yang, C. Janiak, Confinement effects in zeolite-confined noble metals, Angew. Chem. Int. Ed. 58 (36) (2019) 12340–12354.
[33] M. Fan, W.D. Wang, Y. Zhu, X. Sun, F. Zhang, Z. Dong, Palladium clusters confined in triazinyl-functionalized COFs with enhanced catalytic activity, Appl. Catal. B 257 (2019), 117942.
[34] W. Zhao, Y. Jiao, R. Gao, L. Wu, S. Cheng, Q. Zhuang, A. Xie, W. Dong, Sulfonate-grafted conjugated microporous polymers for fast removal of cationic dyes from water, Chem. Eng. J. 391 (2020), 123591.
[35] Q. Zhuang, R. Gao, M. Shi, X. Lin, A. Xie, W. Dong, Confining palladium nanoparticles in microporous tetrastyrene polymer enables efficient size-selective heterogeneous catalysis, ACS Applied Nano Materials 4 (4) (2021) 3869–3876.
[36] L. Wang, Y. Wan, Y. Ding, S. Wu, Y. Zhang, X. Zhang, G. Zhang, Y. Xiong, X. Wu, J. Yang, H. Xu, Conjugated microporous polymer nanosheets for overall water splitting using visible light, Adv. Mater. 29 (2017) 1702428/1702421-1702428.
[37] B. Liang, H. Wang, X. Shi, B. Shen, X. He, Z.A. Ghazi, N.A. Khan, H. Sin, A. M. Khattak, L. Li, Z. Tang, Microporous membranes comprising conjugated polymers with rigid backbones enable ultrafast organic-solvent nanofiltration, Nat. Chem. 10 (9) (2018) 961–967.
[38] C. Yang, Z. Cheng, G. Divitini, C. Qian, B.o. Hou, Y. Liao, A Ni or Co single atom anchored conjugated microporous polymer for high-performance photocatalytic hydrogen evolution, J. Mater. Chem. A 9 (35) (2021) 19894–19900.
[39] S. Luo, Z. Zeng, G. Zeng, Z. Liu, R. Xiao, P. Xu, H. Wang, D. Huang, Y. Liu, B. Shao, Q. Liang, D. Wang, Q. He, L. Qin, Y. Fu, Recent advances in conjugated microporous polymers for photocatalysis: Designs, applications, and prospects, J. Mater. Chem. A 8 (14) (2020) 6434–6470.
[40] S. Luo, Z. Zeng, H. Wang, W. Xiong, B. Song, C. Zhou, A. Duan, X. Tan, Q. He, G. Zeng, Z. Liu, R. Xiao, Recent progress in conjugated microporous polymers for clean energy: Synthesis, modification, computer simulations, and applications, Prog. Polym. Sci. 115 (2021), 101374.
[41] H. Wang, B. Hou, Y. Yang, Q. Chen, M. Zhu, A. Thomas, Y. Liao, Water splitting: Cobalt nanocrystals encapsulated in heteroatom-rich porous carbons derived from conjugated microporous polymers for efficient electrocatalytic hydrogen evolution, Small 14 (2018) 1870193.
[42] H.-L. Cao, H.-B. Huang, Z. Chen, B. Karadeniz, J. Lü, R. Cao, Ultrafine silver nanoparticles supported on a conjugated microporous polymer as high-performance nanocatalysts for nitrophenol reduction, ACS Appl. Mater. Inter. 9 (6) (2017) 5231–5236.
[43] Y. Liao, Z. Cheng, W. Zuo, A. Thomas, C.F.J. Faul, Nitrogen-rich conjugated microporous polymers: Facile synthesis, efficient gas storage, and heterogeneous catalysis, ACS Appl. Mater. Inter. 9 (2017) 38390–38400.
[44] W. Gong, Q. Wu, G. Jiang, G. Li, Ultrafine silver nanoparticles supported on a covalent carbazole framework as high-efficiency nanocatalysts for nitrophenol reduction, J. Mater. Chem. A 7 (22) (2019) 13449–13454.
[45] J.-X. Jiang, C. Wang, A. Laybourn, T. Hasell, R. Clowes, Y.Z. Khimyak, J. Xiao, S. J. Higgins, D.J. Adams, A.I. Cooper, Metal-organic conjugated microporous polymers, Angew. Chem. Int. Ed. 50 (5) (2011) 1072–1075.
[46] C.-C. Hou, T.-T. Li, S. Cao, Y. Chen, W.-F. Fu, Incorporation of a Ru(dcbpy)(bpy)(2)(2+) photosensitizer and a Pt(dcbpy)Cl-2 catalyst into metal-organic frameworks for photocatalytic hydrogen evolution from aqueous solution, J. Mater. Chem. A 3 (19) (2015) 10386–10394.
[47] D.M. D'Souza, D.A. Leigh, M. Papmeyer, S.L. Woltering, A scalable synthesis of 5,5′-dibromo-2,2′-bipyridine and its stepwise functionalization via Stille couplings, Nat. Protoc. 7 (11) (2012) 2022–2028.
[48] J.-X. Jiang, F. Su, A. Trewin, C. Wood, N. Campbell, H. Niu, C. Dickinson, A. Ganin, M. Rosseinsky, Y. Khimyak, A. Cooper, Conjugated microporous poly (aryleneethynylene) networks, Angew. Chem. Int. Ed. 46 (45) (2007) 8574–8578.
[49] P. Mu, W. Bai, Z. Zhang, J. He, H. Sun, Z. Zhu, W. Liang, A.n. Li, Robust aerogels based on conjugated microporous polymer nanotubes with exceptional mechanical strength for efficient solar steam generation, J. Mater. Chem. A 6 (37) (2018) 18183–18190.
[50] P. Mu, Z. Zhang, W. Bai, J. He, H. Sun, Z. Zhu, W. Liang, A. Li, Superwetting monolithic hollow-carbon-nanotubes aerogels with hierarchically nanoporous structure for efficient solar steam generation, Adv. Energy Mater. 9 (2019) 1802158.
[51] C. Kaes, M.W. Hosseini, C.E.F. Rickard, B.W. Skelton, A.H. White, Synthesis and structural analysis of a helical coordination polymer formed by the self-assembly of a 2,2′-bipyridine-based exo-ditopic macrocyclic ligand and silver cations, Angew. Chem. Int. Ed. 37 (7) (1998) 920–922.
[52] G. Jana, S. Pan, P.K. Chattaraj, Binding of small gas molecules by metal–bipyridyl monocationic complexes (metal = Cu, Ag, Au) and possible bond activations therein, The Journal of Physical Chemistry A 121 (19) (2017) 3803–3817.
[53] M. Takenaka, Y. Hashimoto, T. Iwasa, T. Taketsugu, G. Seniutinas, A. Balčytis, S. Juodkazis, Y. Nishijima, First principles calculations toward understanding SERS of 2,2′-bipyridyl adsorbed on Au, Ag, and Au–Ag nanoalloy, J. Comput. Chem. 40 (8) (2019) 925–932.
[54] A. Li, H.-X. Sun, D.-Z. Tan, W.-J. Fan, S.-H. Wen, X.-J. Qing, G.-X. Li, S.-Y. Li, W.-Q. Deng, Superhydrophobic conjugated microporous polymers for separation and adsorption, Energy Environ. Sci. 4 (2011) 2062–2065.
[55] S. Wang, X. Yang, H. Hou, X. Ding, S. Li, F. Deng, Y. Xiang, H. Chen, Highly efficient visible light induced photocatalytic activity of a novel in situ synthesized conjugated microporous poly(benzothiadiazole)–C3N4 composite, Catal, Sci. Technol. 7 (2) (2017) 418–426.
[56] R.-X. Yang, T.-T. Wang, W.-Q. Deng, Extraordinary capability for water treatment achieved by a perfluorous conjugated microporous polymer, Sci. Rep. 5 (2015) 10155.
[57] F. Wang, F. Ren, P. Mu, Z. Zhu, H. Sun, C. Ma, C. Xiao, W. Liang, L. Chen, A.n. Li, Hierarchical porous spherical-shaped conjugated microporous polymers for the efficient removal of antibiotics from water, J. Mater. Chem. A 5 (22) (2017) 11348–11356.
[58] R. Dawson, A. Laybourn, R. Clowes, Y.Z. Khimyak, D.J. Adams, A.I. Cooper, Functionalized conjugated microporous polymers, Macromolecules 42 (22) (2009) 8809–8816.
[59] C. Moreno-Castilla, F. Carrasco-Marín, A. Mueden, The creation of acid carbon surfaces by treatment with (NH4)2S2O8, Carbon 35 (10-11) (1997) 1619–1626.
[60] J. Chun, J.H. Park, J. Kim, S.M. Lee, H.J. Kim, S.U. Son, Tubular-shape evolution of microporous organic networks, Chem. Mater. 24 (17) (2012) 3458–3463.
[61] L. Bao, H. Sun, Z. Zhu, W. Liang, P. Mu, J. Zang, A. Li, Synthesis and properties of tubular-shape conjugated microporous polymers with high purity, Mater. Lett. 178 (2016) 5–9.
[62] P. Mu, W. Bai, Y. Fan, Z. Zhang, H. Sun, Z. Zhu, W. Liang, A.n. Li, Conductive hollow kapok fiber-PPy monolithic aerogels with excellent mechanical robustness for efficient solar steam generation, J. Mater. Chem. A 7 (16) (2019) 9673–9679.
[63] Q. Zhuang, C. Zhang, H. Zhuang, H. Deng, X. Lin, Y. Li, H. Chen, A. Xie, W. Dong, Heteroatom-free conjugated tetraphenylethylene polymers for selectively fluorescent detection of tetracycline, Anal. Chim. Acta 1190 (2022), 339236.
[64] J. Zhou, X. Gao, R. Liu, Z. Xie, J. Yang, S. Zhang, G. Zhang, H. Liu, Y. Li, J. Zhang, Z. Liu, Synthesis of graphdiyne nanowalls using acetylenic coupling reaction, J. Am. Chem. Soc. 137 (24) (2015) 7596–7599.
[65] J. Kim, C.M. Moisanu, C.N. Gannett, A. Halder, J.J. Fuentes-Rivera, S.H. Majer, K. M. Lancaster, A.C. Forse, H.D. Abruña, P.J. Milner, Conjugated microporous polymers via solvent-free ionothermal cyclotrimerization of methyl ketones, Chem. Mater. 33 (21) (2021) 8334–8342.
[66] Y.a. Yan, S.-Z. Kang, J. Mu, Preparation of high quality Ag film from Ag nanoparticles, Appl. Surf. Sci. 253 (10) (2007) 4677–4679.
[67] X. Hu, S. Lu, J. Tian, N. Wei, X. Song, X. Wang, H. Cui, The selective deposition of MoS2 nanosheets onto (101) facets of TiO2 nanosheets with exposed (001) facets and their enhanced photocatalytic H-2 production, Appl. Catal. B 241 (2019) 329–337.
[68] K. Wang, J. Li, G. Zhang, Ag-bridged Z-scheme 2D/2D Bi5FeTi3O15/g-C3N4 heterojunction for enhanced photocatalysis: Mediator-induced interfacial charge transfer and mechanism insights, ACS Appl. Mater. Inter. 11 (2019) 27686–27696.
[69] C. Levard, E.M. Hotze, G.V. Lowry, G.E. Brown, Environmental transformations of silver nanoparticles: Impact on stability and toxicity, Environ. Sci. Technol. 46 (2012) 6900–6914.
[70] S. Vasileiadis, G. Brunetti, E. Marzouk, S. Wakelin, G.A. Kowalchuk, E. Lombi, E. Donner, Silver toxicity thresholds for multiple soil microbial biomarkers, Environ. Sci. Technol. 52 (15) (2018) 8745–8755.
[71] Y. Gao, W. Wu, K. Qiao, J. Feng, L. Zhu, X. Zhu, Bioavailability and toxicity of silver nanoparticles: Determination based on toxicokinetic–toxicodynamic processes, Water Res. 204 (2021), 117603.
[72] Y. Liu, K. Zhang, W. Li, J. Ma, G.J. Vancso, Metal nanoparticle loading of gel-brush grafted polymer fibers in membranes for catalysis, J. Mater. Chem. A 6 (17) (2018) 7741–7748.
[73] J. Xu, X. Zheng, Z. Feng, Z. Lu, Z. Zhang, W. Huang, Y. Li, D. Vuckovic, Y. Li, S. Dai, G. Chen, K. Wang, H. Wang, J.K. Chen, W. Mitch, Y.i. Cui, Organic wastewater treatment by a single-atom catalyst and electrolytically produced H2O2, Nature Sustainability 4 (3) (2021) 233–241.
[74] F. Pan, F. Xiao, N. Wang, Towards application of a covalent organic framework-silver nanoparticles@sand heterostructure as a high-efficiency catalyst for flow-through reduction of organic pollutants, Appl. Surf. Sci. 565 (2021), 150580.
[75] R. Du, N. Zhang, H. Xu, N. Mao, W. Duan, J. Wang, Q. Zhao, Z. Liu, J. Zhang, CMP aerogels: Ultrahigh-surface-area carbon-based monolithic materials with superb sorption performance, Adv. Mater. 26 (2014) 8053–8058.

[76] R. Subair, B.P. Tripathi, P. Formanek, F. Simon, P. Uhlmann, M. Stamm, Polydopamine modified membranes with in situ synthesized gold nanoparticles for catalytic and environmental applications, Chem. Eng. J. 295 (2016) 358–369.
[77] Z.-C. Xiong, Z.-Y. Yang, Y.-J. Zhu, F.-F. Chen, R.-L. Yang, D.-D. Qin, Ultralong hydroxyapatite nanowire-based layered catalytic paper for highly efficient continuous flow reactions, J. Mater. Chem. A 6 (14) (2018) 5762–5773.
[78] N. Wang, F. Wang, F. Pan, S. Yu, D. Pan, Highly efficient silver catalyst supported by a spherical covalent organic framework for the continuous reduction of 4-nitrophenol, ACS Appl. Mater. Inter. 13 (2) (2021) 3209–3220.